The smallest stroke: occlusion of one penetrating vessel leads to infarction and a cognitive deficit

Andy Y Shih[1,5], Pablo Blinder[1,5], Philbert S Tsai[1], Beth Friedman[2], Geoffrey Stanley[1], Patrick D Lyden[3] & David Kleinfeld[1,4]

Microinfarctions are present in the aged and injured human brain. Their clinical relevance is controversial, with postulated sequelae ranging from cognitive sparing to vascular dementia. To address the consequences of microinfarcts, we used controlled optical methods to create occlusions of individual penetrating arterioles or venules in rat cortex. Single microinfarcts, targeted to encompass all or part of a cortical column, impaired performance in a macrovibrissa-based behavioral task. Furthermore, the targeting of multiple vessels resulted in tissue damage that coalesced across cortex, even though the intervening penetrating vessels were acutely patent. Post-occlusion administration of memantine, a glutamate receptor antagonist that reduces cognitive decline in Alzheimer's disease, ameliorated tissue damage and perceptual deficits. Collectively, these data imply that microinfarcts likely contribute to cognitive decline. Strategies that have received limited success in the treatment of ischemic injury, which include therapeutics against excitotoxicity, may be successful against the progressive nature of vascular dementia.

Cognitive impairment as a consequence of age or injury has many root causes. Evidence from aged patients suggests that a common basis for cognitive decline involves the disruption of the microvasculature of the brain[1–3]. Post-mortem studies of patients with dementia have identified, in addition to other pathologies, an abundance of cortical microinfarcts[4–7] with diameters on the order of 0.1–1 mm (**Fig. 1a**). These microinfarcts are often juxtaposed to a variety of angiopathies, including hyaline arteriosclerosis, full and partially occluded vessel lumens, and inflamed vascular walls[4]. However, *in vivo* studies that seek to establish whether such microinfarcts occur concurrently with cognitive decline, or are even predictive of decline, are hampered by an inability to resolve such small lesions with conventional non-invasive imaging[2]. Thus, it is not clear whether microinfarcts are largely benign or are a contributing factor. This implies the need for an experimental model for directly examining the consequences of small vessel thrombosis in cortex and to serve as a test bed for treatments to mitigate cognitive impairment secondary to vascular disease.

The topology of rodent cortical angioarchitecture[8] has essential features that appear similar to that of humans[9]. This supports the utility of a rodent model for examining whether thrombosis of individual small cortical vessels could be the basis of microinfarction and whether strokes on such a small scale can negatively affect cognition. In this regard, we focus on penetrating vessels, the arterioles and venules that shuttle blood between the cortical surface and the parenchyma[10]. Past studies have found that penetrating arterioles[11] and venules[12] form bottlenecks in the supply of blood to neighborhoods of microvessels. This highlights the penetrating vessel as a locus of vulnerability during vascular disease[8,11,12]. Loss of flow to even

a single cortical penetrating arteriole will generate a nominally cylindrical microinfarction that can extend through the full depth of cortex[8,13] (**Fig. 1b**). The small strokes in rodent appear to match human microinfarcts in geometry[14] (**Fig. 1**) and in the ability to induce a local inflammatory response, consistent with the correspondence in size between rodent and primate cortical microvessels[15,16].
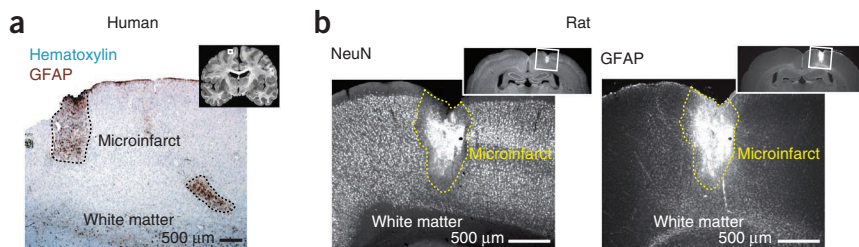
We addressed the potential cognitive effect of microinfarctions using a rodent model of targeted micro-occlusions. Our overarching aim was to unravel the so-called silent features of microinfarcts in progressive cognitive decline, as well as to address their etiology and response to pharmacological intervention. We asked how the extent of cortical microinfarction is shaped by features such as vascular topology, blood volume flux and the type of vessel, whether the occlusion of single cerebral vessel can lead to cognitive impairment, how the accumulation of multiple small vessel occlusions affects tissue integrity, and what therapeutic agents may obviate the extent and potential effect of microinfarctions.

RESULTS

We used *in vivo* two-photon laser-scanning microscopy[17] to visualize blood vessels and neurons through a cranial window in the somatosensory cortex of anesthetized rats[18]. Each cubic millimeter of rat cortex contains an average of six penetrating arterioles and 16 penetrating venules ($n = 9$ rats). The penetrating vessels originated as branches from the surface vasculature and dived radially into the parenchyma (**Fig. 2a**). We categorized all vessels into three groups: penetrating arterioles, penetrating venules and deep microvessels (that is, vascular segments that ramify from the penetrating vessel

Figure 1 Similarity between human and rat cortical microinfarcts. (**a**) Histology of microinfarcts detected in the cortex of an elderly human. The infarcted area is dense with reactive astrocytes that stained with glial fibrillary acidic protein (GFAP, brown). The tissue was counterstained with hematoxylin (blue). Adapted from ref. 14. (**b**) Microinfarct as seen 7 d after occlusion of a single penetrating arteriole in rat cortex. Neuronal viability was assessed with antibody to NeuN and astrogliosis was assessed with antibody to GFAP. Adapted from ref. 8.

below the pial surface). Each type of vessel was found to be associated with a range of lumen diameters and red blood cell (RBC) velocities; we used these parameters to calculate volume flux through the vessel. Penetrating vessels supported values of flux[19] predominantly from 100 pl s^{-1} to 10 nl s^{-1}, whereas deep microvessels supported values primarily between 1 and 100 pl s^{-1} (**Fig. 2b**). The population of deep microvessels was further analyzed as vessel subtypes (**Supplementary Fig. 1a–d**), but was pooled here for clarity. We considered the tissue damage that resulted from occlusion of an individual vessel in each of these categories.

Our implementation of *in vivo* two-photon microscopy permitted us to form clots in targeted, individual blood vessels that lie both on and below the brain surface using two complementary techniques[20]. Penetrating vessels were occluded near the cortical surface by linear absorption of focused green laser light in the presence of a circulating photosensitizer, Rose Bengal[21]. Occlusion of the vascular lumen was completed in 60–90 s. Deep microvessels were occluded by nonlinear absorption of amplified, ultrashort laser pulses to generate highly focused irradiation without affecting tissue above or below the target vessel[22]. Occlusion of the microvascular lumen was completed in 120 s.

Acute consequences of single penetrating vessel occlusion

What is the time window for the onset of neuronal deficits? To answer this, we investigated the acute consequences of single penetrating vessel clots. We first used *in vivo* imaging of neuronal [Ca^{2+}] by two-photon microscopy[17] to assess the loss of functionally evoked neuronal activity in the core of the microinfarct. For this, we imaged in the relatively large hindlimb region of the primary somatosensory cortex, where peripheral electrical stimulation could reliably activate a large number of neurons. We loaded the Ca^{2+}-sensitive dye Oregon Green Bapta-AM (OGB1-AM) intracortically[23] and quantified the activity of layer 2/3 neurons in response to limb stimulation as a function of time after clot formation (**Fig. 3a–e**).

The number of neurons responsive to hindlimb stimulation was found to decrease precipitously in the first 2 h after occlusion of a single penetrating arteriole (**Fig. 3c**). A similar effect was observed following occlusion of a single penetrating venule (**Fig. 3d**). As a control, Ca^{2+}-sensitive dye was also loaded into the region that represents forelimb, which lies more than 1 mm away from the hindlimb region. The forelimb area remained responsive to stimulation over a period of 3 h, indicating that stroke-induced loss of function did not result from a general metabolic run-down of the rats (**Fig. 3e**). The occluded vessel was periodically monitored to ensure that the clot remained stable over the entire imaging period.

Consistent with a loss of neural function in the core of the microinfarct, occlusion of either a penetrating arteriole or venule generated severely hypoxic conditions in the acute period of 6 h post-occlusion, that is, pO$_2$ < 10 mm Hg, as reported by α-hypoxyprobe staining in *post hoc* histology[19] (**Fig. 3f**). The hypoxic tissue overlapped precisely with a column of severe vascular pathology in the microinfarct core (**Fig. 3f**), as highlighted by retention of the circulating fluorescein-dextran in the endothelia of the deep microvasculature[24]. In addition, the microinfarct core exhibited increased labeling with α-3-nitrotyrosine, indicative of oxidative protein damage in cells and vasculature[25], as well as reduced α-aquaporin-4 staining and increased rat α-immunoglobulin G staining, indicative of pathology in astrocytes and blood brain barrier leakage[26], respectively (**Supplementary Fig. 2**). The border of the infarct was not spared from pathology, as it was delineated with propidium iodide–positive cells[27] (**Fig. 3g**); this is indicative of membrane degradation. We further noted reactivity with the macrophage marker α-CD68 both inside and outside of the core of the microinfarct (**Fig. 3h**). Staining for CD68 is a common marker for clinical microinfarcts[28]. Finally, a wall of microglial processes was observed along the stroke border, presumably as a response to limit the damage (**Supplementary Fig. 3**).

The finding that occlusion of a single penetrating vessel, whether arteriolar or venular, leads to multiple hallmarks of ischemic injury (**Fig. 3f–h** and **Supplementary Figs. 2** and **3**) is suggestive of an outward spread of cell death with a receding penumbra. In support of this hypothesis, we observed waves of increasing intracellular [Ca^{2+}] propagating outward from the core of the microinfarct across several hundred micrometers in response to penetrating arteriole occlusion, indicative of spreading depression[29] (**Fig. 3i**). The velocity of these events, 30–70 μm s^{-1}, were similar to those seen in previous *in vivo* imaging studies[30].

Microinfarction following single penetrating vessel clot

The occlusion of a single penetrating arteriole leads to a highly localized, nominally cylindrical region of tissue infarction over a course of 7 d[8], as reproduced here (**Fig. 4**) and delineated by a region devoid of staining for the pan-neuronal marker NeuN in neuronal somata
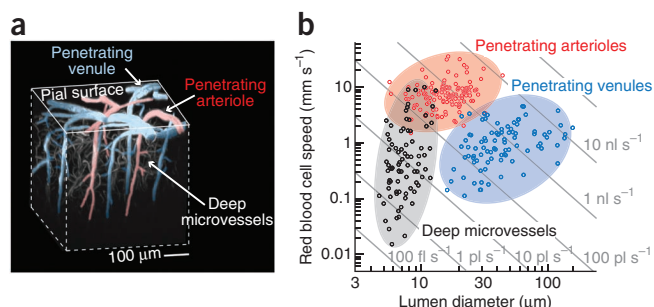
Figure 2 Topology and flow dynamics of cortical vasculature. (**a**) Three-dimensional reconstruction of cortical vasculature in a 0.5-mm^3 tissue volume collected from rat cortex *in vivo*. Penetrating arterioles (red) plunged into cortex to feed the deep microvasculature (white), whereas penetrating venules drained blood back toward the pial surface (blue). (**b**) Dynamics of RBC speed and lumen diameter collected from single vessels. The gray lines correspond to constant RBC volume flux.
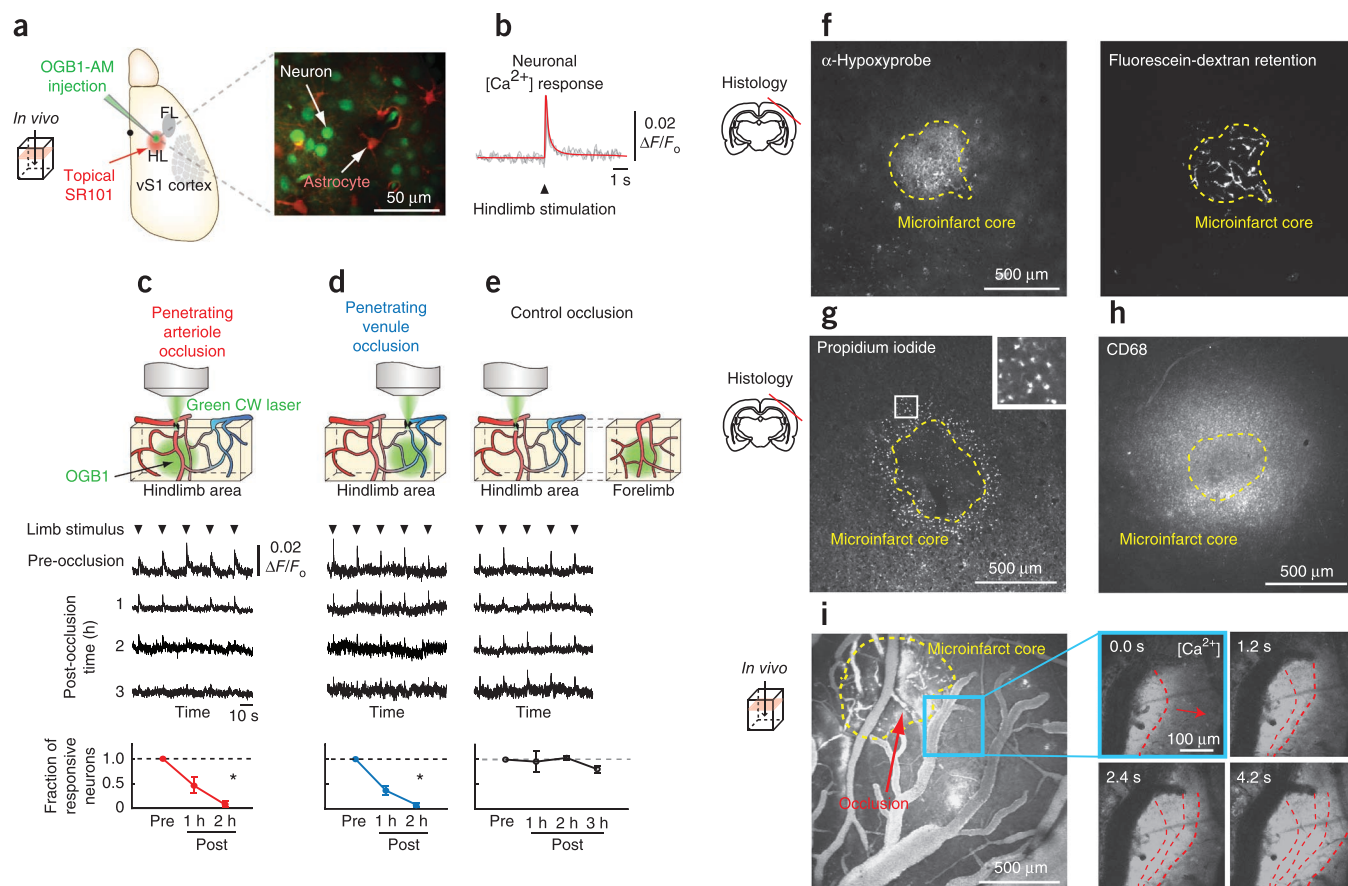
Figure 3 Acute neuropathology and growth of microinfarcts. (**a**) *In vivo* two-photon imaging of neuronal activity in the limb region of somatosensory cortex that was loaded with the Ca^{2+} indicator OGB1-AM and the astrocyte-specific dye SR101. FL, forelimb; HL, hindlimb. (**b**) $[Ca^{2+}]$ responses from individual layer 2/3 neurons evoked by hindlimb stimulation. (**c**) Occlusion of a single penetrating arteriole gradually decreased the responsiveness of local neurons. Bottom, the proportion of responsive neurons plotted as a function of time post-occlusion. Line graphs are presented as mean ± s.e.m. ($n = 4$, *$P = 0.015$ compared to baseline). CW, continuous wave. (**d**) Occlusion of a single penetrating venule gradually decreased the responsiveness of local neurons. Bottom, the proportion of responsive neurons over time ($n = 5$, *$P = 0.014$ compared with baseline). (**e**) Distant control region in the same cranial window (forelimb), also loaded with OGB1-AM, revealed no loss of neuronal responsiveness following occlusion in hindlimb cortex ($n = 4$). (**f**) Histological examination of microinfarcts 6 h post-occlusion. Tissue hypoxia, identified with Hypoxyprobe ($n = 6$ of each vessel type), overlapped with endothelial retention of fluorescein-dextran in the microinfarct core (yellow dashed line). (**g**) Ring of necrotic cells, as highlighted by propidium iodide uptake, delineated the microinfarct border ($n = 4$ of each vessel type). (**h**) CD68 staining of inflammatory cells ($n = 11$ of each vessel type). (**i**) Wave of cortical spreading depression, moving at 30 µm s^{-1}, observed by *in vivo* $[Ca^{2+}]$ imaging (red dashed line, right) after occlusion of a single penetrating arteriole (red arrow, left). The Ca^{2+} wave was observed 30 min post-occlusion. The inset in the right panel (blue border) shows a time course of magnified images.

(**Figs. 1b** and **4a** and **Supplementary Fig. 4a**), and by the local proliferation of reactive astrocytes (**Fig. 1b** and **Supplementary Fig. 4a**). The chronic result of occlusion to a penetrating venule is unreported and not readily predicted, as penetrating venules outnumber arterioles in rodent cortex and are highly collateralized on the pial surface[12]. Indeed, occlusion of a penetrating venule generated a microinfarction with notable similarity to that caused by occlusion of a penetrating arteriole, as seen with the loss of staining for NeuN (**Fig. 4b** and **Supplementary Fig. 4b**) and reactive astrogliosis (**Supplementary Fig. 4b**). Both microinfarct types exhibited dense packing of Nissl bodies, indicative of a gliotic, sub-acute lesion (**Supplementary Fig. 4c,d**). The penetrating arteriole and venule microinfarcts spanned, respectively, diameters of 460 ± 70 µm (mean ± s.d.) and 500 ± 120 µm and depths of 1.17 ± 0.32 mm and 1.30 ± 0.25 mm relative to the pia to yield the statistically identical microinfarct volumes of 220 ± 140 nl and 210 ± 100 nl ($P = 0.85$, unpaired t test). The volume of infarction was correlated with the pre-occlusion flux of RBCs through the vessel (**Fig. 4d**); occlusion of vessels with

greater flux led to larger microinfarcts. These data indicate that there is an approximate equivalence, in terms of microinfarct generation, between occlusion of penetrating arterioles and venules.

In contrast with the case for penetrating vessels, the tissue infarction detected after occlusion of deep microvessels was minute (**Fig. 4c,e**). The targeted microvessels included direct branches of a source penetrating vessel or vessels that were two or more branch points distant to the penetrating vessel; endothelial retention of fluorescein-dextran served as a sensitive indicator of the targeted microvessel during histology[22]. We again assayed for small regions of necrotic damage using nuclear uptake of propidium iodide by dying cells[27]. We found that occlusion of those microvessels that were direct branches from the source penetrating vessel, that is, subsurface arterioles or venules, generated extremely small and transient regions of tissue damage, with a maximum infarct volume of 0.8 nl (**Fig. 4e** and **Supplementary Fig. 1e**). However, occlusion of microvessels that were two or more branch points from the penetrating vessel, that is, capillaries, resulted in no detectable tissue damage (**Fig. 4e** and

Figure 4 Chronic nature of microinfarcts caused by occlusion of penetrating arterioles and venules in rat cortex. (**a–c**) Microinfarcts that resulted from occlusion of single vessels. Each column shows a cartoon of the method of vascular occlusion (top), planar two-photon images of the target vessel before and after occlusion (middle), and assessment of tissue viability by NeuN immunohistochemistry 7 d post-occlusion (bottom). (**d**) Scatter plot of the microinfarct volume versus the pre-occlusion RBC volume flux of individual penetrating vessels. Microinfarct volume was correlated with flux; $R = 0.8$ ($n = 11$, $P = 0.0039$) for arterioles and $R = 0.7$ ($n = 8$, $P = 0.049$) for venules. The data follow a power law (fit lines) with volume $\propto$ (flux)^n, where $n = 0.33 \pm 0.05$ (mean slope $\pm$ s.d.) and 0.12 ± 0.02 for arterioles and venules, respectively. The crossbars show mean $\pm$ s.e.m. for all data points in each vessel group. (**e**) Scatter plot of damage volume versus pre-occlusion RBC flux for individual deep microvessels. The crossbar shows mean $\pm$ s.e.m., excluding data points with microinfarct volumes of zero.
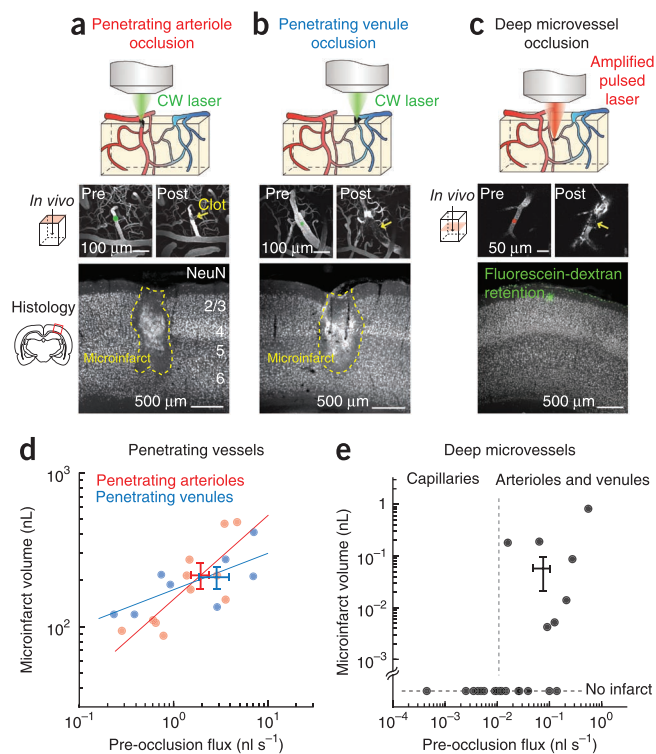
Supplementary Fig. 1f). These findings are consistent with a cyclically connected microvascular network, where flow in downstream vascular branches can reverse to compensate for loss of flow after clot formation[22]. As occlusion of deep microvessels caused negligible damage in comparison with penetrating vessels, such lesions were not studied further.

Attenuation of microinfarct growth by NMDAR antagonists

We speculate that the acute expansion of the infarction, particularly as it involves excitotoxic waves (**Fig. 3i**), may be amenable to therapeutic intervention. Thus, we tested whether administration of neuroprotective agents after the onset of an infarction could mitigate its growth. Antagonists of NMDA-type glutamate receptors (NMDARs) are potential therapeutic agents for age-related pathologies that are thought to involve excitotoxicity, such as vascular dementia[31] and neurodegeneration[32]. We investigated the effect of a noncompetitive glutamate receptor antagonist, MK-801, and a moderate-affinity noncompetitive glutamate receptor antagonist, memantine, on microinfarct volumes induced by single penetrating vessel occlusions (**Fig. 5a–c**). Both antagonists, delivered by intraperitoneal injection, were found to be highly effective at reducing microinfarct volumes caused

by occlusion of either a penetrating arteriole (**Fig. 5d**) or venule (**Fig. 5e**). Notably, memantine was administered 30–45 min after the initiation of occlusions.

Summary statistics across all occlusions without and with NMDAR antagonists revealed that the median radius of the infarct was reduced from 230 to 50 μm (**Fig. 5f**), which indicates a relatively large volume of salvageable penumbra. It is of interest that the maximum radius of the infarct, about 310 μm, was close to the distance from the occlusion at which normal flow of RBCs in microvessels in layer 2/3 of cortex was reestablished (**Fig. 5f**). Furthermore, the minimum radius of damage

Figure 5 Reduction in the volume of isolated microinfarcts by administration of NMDAR antagonists. (**a–c**) Two NMDAR antagonists, MK-801 and memantine (Mem), reduced microinfarct volume. Representative images of infarcted tissue, as assessed by NeuN immunohistochemistry, over a depth of 800 μm below the pial surface. (**d**) Volume of isolated microinfarcts that resulted from occlusion of individual penetrating arterioles in each treatment group. Bar graphs are presented as mean $\pm$ s.d. ($n = 11$, 8 and 7 for control, MK-801 and memantine, respectively; *$P = 0.006$ for control versus MK-801 and **$P = 0.003$ for control versus memantine). Pre-occlusion RBC volume fluxes of targeted vessels were not statistically different between groups ($P = 0.44$). Individual data points (open circles) are shown for each bar of the bar graphs. (**e**) Volume of isolated infarct that resulted from occlusion of individual penetrating venules in

each treatment group ($n = 8$, 7 and 16 for control, MK-801 and memantine, respectively; #$P < 0.0001$ for control versus MK-801 and ##$P = 0.002$ for control versus memantine). Pre-occlusion RBC fluxes of targeted vessels were not statistically different between groups ($P = 0.51$). (**f**) Cumulative probability of the radius of microinfarcts 5–7 d post-occlusion across all occlusion data with and without NMDAR antagonists. Red and blue curves correspond to penetrating arterioles and venules, respectively. Note the reduction in size of the microinfarcts by treatment with antagonists. The pink curve is the acute decrease in the speed of RBCs in microvessels in layer 2/3 as a function of distance from the occlusion, adapted from ref. 11; data shown as mean $\pm$ s.e.m. (gray).
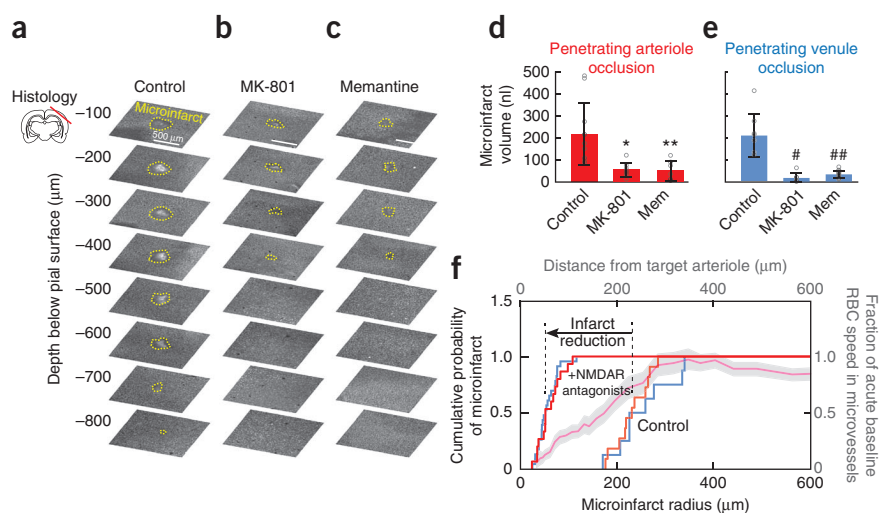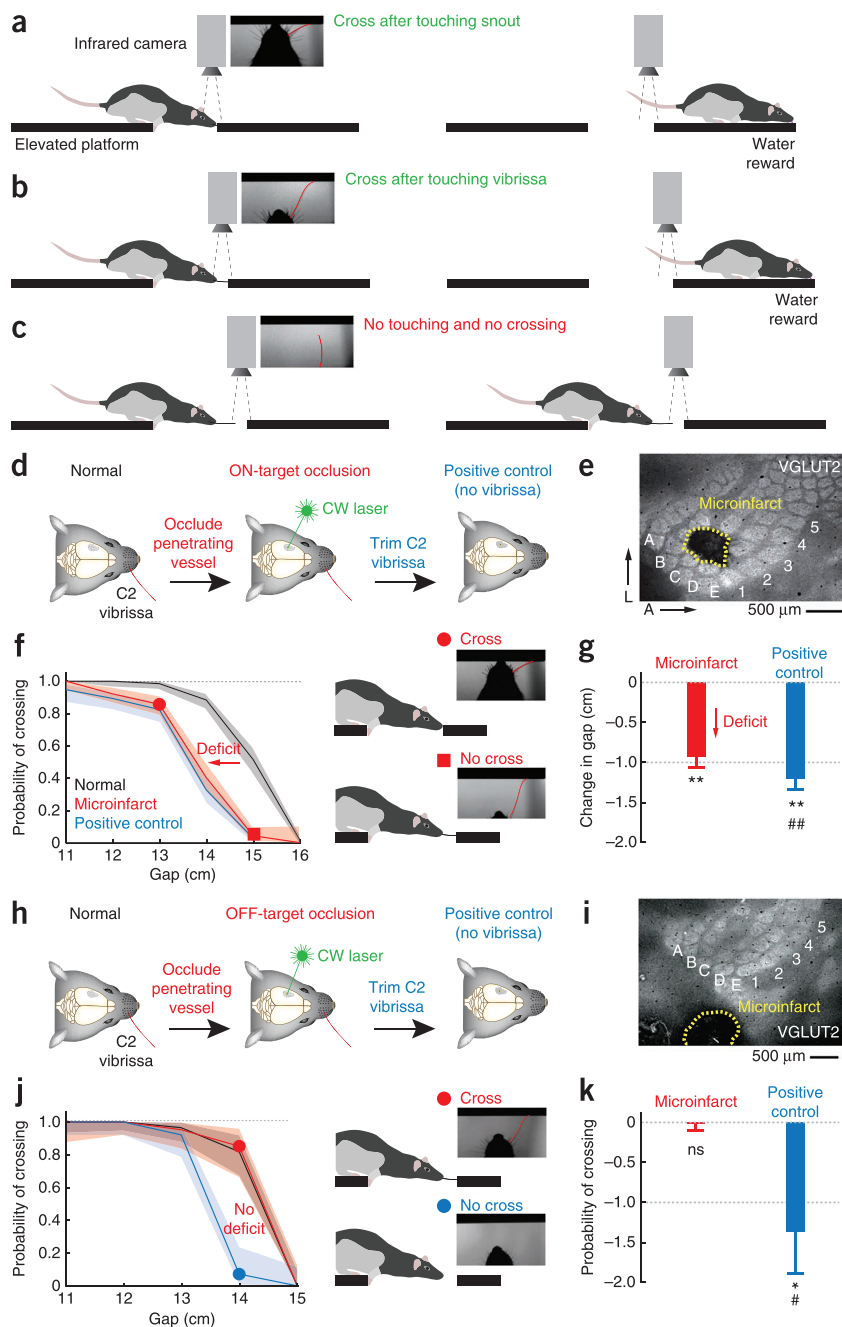
Figure 6 Cognitive deficit following single penetrating vessel occlusion in vibrissa primary sensory cortex. (**a**–**c**) Summary of rat behavior in the gap-crossing task. At short distances, the animal detects the presence of the target platform with its snout (**a**). At intermediate distances, the rat extended its macrovibrissa to detect the platform (**b**). At long distances, the platform was not reachable and the rat did not cross (**c**). The images show vibrissa position in an attempt to contact the target platform during a single trial. (**d**) Experiment to test the effects of an ON-target stroke. (**e**) *Post hoc* histology revealed a microinfarct localized to the C2 column after occlusion of a single penetrating venule. A, anterior; L, lateral. (**f**) Probability of successful crosses at each gap distance, with 0.95 confidence intervals, shown under normal conditions (black curve), following microinfarction (red curve), and following removal of the C2 macrovibrissa (blue curve). (**g**) Summary of gap-crossing deficits of the ON-target cohort. Bar graphs are presented as mean ± s.e.m. ($n = 10$; **$P < 0.0001$ compared to normal conditions and ##$P = 0.008$, compared to post-microinfarct). (**h**–**k**) Control experiment, presented as in **d**–**g**, to test the effects of an OFF-target stroke ($n = 3$; *$P = 0.016$, compared to normal conditions and #$P = 0.016$, compared to post-microinfarct). A nonsignificant (ns) value of $P = 0.99$ was calculated for comparison of microinfarct with normal conditions.

after treatment with either NMDAR antagonist, about 25 µm, corresponds to the radius for which blood flow was completely halted after a single, focal occlusion, that is, the ischemic core (**Fig. 5f**).

## Cognitive deficit following penetrating vessel occlusion

We then asked whether the microinfarction that results from the occlusion of just one penetrating vessel generates a cognitive deficit. To address this question, we used a procedure that involves somatosensation by macrovibrissa, the long hairs that rodents use to sense objects in front of them. The motion of each macrovibrissa is sensed by receptors whose outputs are conveyed predominantly to a single cortical column, roughly 400 µm in diameter, in primary vibrissa sensory (vS1) cortex[33,34]. The task is based on localized sensory input that leads to a cognitive decision and a motor plan,

that is, to cross or not to cross, as opposed to a purely sensory measure.

Rats, with their mystacial pad trimmed down to one macrovibrissa, were trained to cross a gap that separated two elevated platforms for a reward of water[35] (**Fig. 6**). The task was performed in infrared light to remove sight as a potential confound. For relatively small gaps, the rat crossed the opening if the target platform could be contacted with the snout or paw (**Fig. 6a**). For intermediate gap distances, the rat perched at the edge of the platform and extended its macrovibrissa to sense the presence of the target platform before deciding whether to cross (**Fig. 6b**). Use of the macrovibrissa, rather than touching with the snout, allowed the rat to probe an additional distance, between 1 and 2 cm in practice, across the gap. Finally, as the gap was extended further, the rat was incapable of touching the target platform with the extended macrovibrissa and would not attempt to cross the gap lest it fall through the opening (**Fig. 6c**). This task isolated the use of a single macrovibrissa to cross intermediate gap distances and therefore provided readily controlled conditions for testing a perception on the basis of the functionality of the corresponding cortical column.

Once each rat was fully trained, we established a psychometric curve for the probability that the rat would cross a gap as a function of the width of the gap (**Fig. 6d,f,h,j**). This curve established the distance at which the rat had a 0.5 chance of crossing the gap and served as the baseline distance for subsequent comparison for the same rat.

The rats were divided into two cohorts. In the first cohort ($n = 10$; 4 arterioles and 6 venules; **Fig. 6d–g**), identified as ON-target

ARTICLES

Figure 7 Reduction in cognitive deficit following single penetrating vessel occlusion by administration of the NMDAR antagonist memantine. (**a**) Experiment to test the effects of an ON-target stroke followed by treatment with memantine. (**b**) *Post hoc* immunohistochemistry revealed a small microinfarct affecting part of the C2 column after occlusion of a single penetrating venule and treatment. (**c**) Probability of successful crosses at each gap distance, with 0.95 confidence intervals, shown under normal conditions (black curve), following microinfarction plus memantine (red curve), and following removal of the C2 macrovibrissa (blue curve). Note that the rat was only slightly impaired. (**d**) Summary gap-cross deficits of the treated, ON-target cohort. Bar graphs are presented as mean ± s.e.m. ($n = 7$; ***$P < 0.0001$ compared with normal conditions, and ###$P = 0.0006$ compared with post-microinfarct; a nonsignificant (ns) value of $P = 0.1$ was calculated for comparison of microinfarct plus memantine with normal conditions). (**e**) Summary plot across all ON-target occlusion cases, memantine-treated ON-target occlusion cases and OFF-target control cases. Note the strong reduction in size of the behavioral deficit resulting from treatment with memantine, consistent with a reduced fraction of cortical column being infarcted. (**f**) Summary of the gap-cross deficits across all groups revealed that the addition of memantine led to a significant reduction in the cognitive deficit for ON-target occlusion ($n = 3$, 7 and 10 for OFF-target, ON-target plus memantine and ON-target, respectively; *$P = 0.037$, **$P = 0.009$).
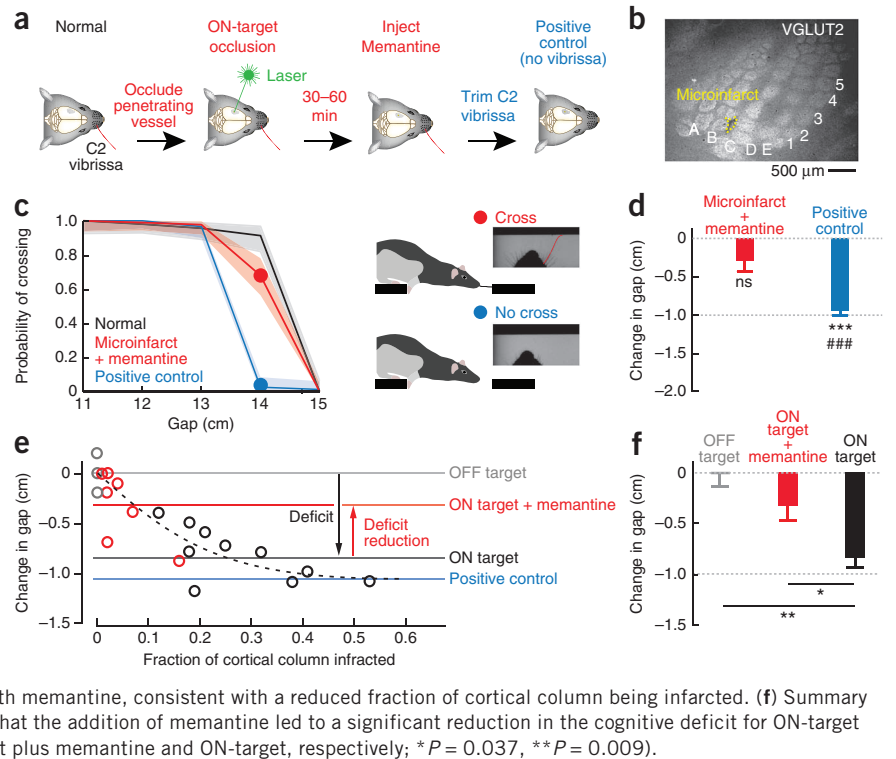
occlusion, vessels targeted for occlusion were selected using intrinsic optical imaging combined with vibrissa stimulation[36] to identify the location of the cortical column that received predominant input from the C1 or C2 macrovibrissa. We then occluded the penetrating vessel, arteriolar or venular, that was best centered in this column (**Fig. 6e** and **Supplementary Fig. 5**) and was expected to generate a microinfarct that encompassed the bulk of the superficial and middle layers of cortex (**Fig. 4a,b**). The rat was then re-assessed in the gap-crossing task at 4–7 d post-occlusion (**Fig. 6f**). In each case, the rat could still perform the task when the gap was short enough for the rat to touch the target platform with its snout (**Fig. 6f**). With larger gaps, however, the rat could no longer detect the target platform, even though videography revealed that the target platform was contacted by the rat's macrovibrissa (**Fig. 6f**). This behavioral deficit, from a single penetrating vessel occlusion, was quantified in terms of a new psychometric curve, which showed that the navigable gap size decreased by about 1 cm for a 0.5 chance of crossing (**Fig. 6f**). Similar results were found across the cohort (**Fig. 6g**). Finally, as a positive control, removal of the single C1 or C2 macrovibrissa in the ON-target cohort resulted in an additional small, ~0.1-cm decrease in the navigable gap size for a 0.5 chance of crossing across the cohort (**Fig. 6g**). This uncovered a small, but substantial, functional compensation that is consistent with palpation that leads to activation of neighboring follicles, with their vibrissa stumps, and corresponding cortical columns[37].

In a second cohort of rats ($n = 3$), occlusions were made to penetrating vessels that supplied regions of cortex distant to the relevant cortical column in vS1 cortex (**Fig. 6h–k**), identified as OFF-target occlusions. These negative control rats showed no gap-crossing deficit as a result of vascular occlusion (**Fig. 6j**). As a positive control for these rats, removal of the single macrovibrissa shifted the psychometric curve by more than 1 cm, as expected given that the rats could no longer touch the target platform (**Fig. 6j**). Similar results were found across the cohort of subjects (**Fig. 6k**).

Rats were killed on the last day of behavioral assessment to allow for histological determination of the location and size of the infarct caused by penetrating vessel occlusion. These data showed that blockade of only a single penetrating vessel was sufficient to ablate an entire cortical column in the vS1 cortex of the ON-target group (**Fig. 6e** and **Supplementary Fig. 5**) and a similarly sized region outside of vS1 cortex for the OFF-target group (**Fig. 6i** and **Supplementary Table 1**). Taken together, these data indicate that a strategically located microinfarct caused by occlusion of a single penetrating vessel leads to a cognitive deficit.

Cognitive deficits are diminished by memantine
The volume of microinfarcts secondary to occlusion of a penetrating vessel was substantially reduced by treatment with NMDAR antagonists (**Fig. 5**). We tested whether these therapeutic agents could provide an additional beneficial effect on reducing cognitive deficits secondary to an occlusion (**Fig. 6**). We used the gap-crossing task with ON-target occlusion (**Fig. 6d–g**) and administered memantine 30–45 min after the occlusion (**Fig. 7a**). The rats were then assessed in the task for an additional 4–7 d post-occlusion. These rats, treated with memantine, were able to cross essentially the same gap that was navigable before the occlusion (**Fig. 7c,d**). Removal of the remaining vibrissa as a positive control restored the full deficit in the example shown (**Fig. 7c**), and in general across the cohort ($n = 7$; **Fig. 7d** and **Supplementary Table 1**).

The fraction of a cortical column that was affected by a penetrating vessel occlusion depended on the location and geometry of the microinfarct. The group of all ON-target data included microinfarcts that were roughly centered in the column; those for which memantine was administered tended to be much smaller, and the resultant microinfarcts often covered only a small fraction of the target column (**Fig. 7b** and **Supplementary Table 1**). A plot of the perceptual deficit versus the measured fraction of the infarcted

2013 Nature America, Inc. All rights reserved.

VOLUME 16 | NUMBER 1 | JANUARY 2013 **NATURE NEUROSCIENCE**

Figure 8 Potential coalescence of multiple, single penetrating vessel microinfarcts into an extended infarct. (**a**) Single penetrating vessel occlusions placed distantly from each other form isolated microinfarcts. Top, wide-field view of vasculature as imaged by *in vivo* two-photon microscopy. The locations of occluded vessels are marked with a blue circle, with the area of the circle approximating the predicted microinfarct area, and a letter to indicate the target vessel type (A, one penetrating arteriole; V, one penetrating venule). Middle, the actual microinfarct boundary at 7 d post-occlusion, as assessed by NeuN staining. Bottom, predicted microinfarct regions overlaid with the actual microinfarct size. A, anterior; M, medial. (**b**) Multiple penetrating vessel occlusions placed in close proximity coalesce into larger infarcts. (**c**) Gradual loss of flow in intervening penetrating vessels revealed by longitudinal imaging. Non-flowing vessel segments (red) are marked as a function of time on a planar image collected pre-occlusion. (**d**,**e**) Coalescence of microinfarcts was blocked by administration of MK-801 or memantine. (**f**) Pre-occlusion RBC fluxes of targeted vessels were not statistically different between groups. Bar graphs are presented as mean ± s.d. (n = 7, 3 and 6 for control, MK-801 and memantine, respectively; P = 0.97). Individual data points (open circles) are shown for each bar of the bar graphs. (**g**) Final microinfarct volumes were statistically different between groups (**P = 0.0054 and *P = 0.023, compared with control). (**h**) The probability of coalescence in control and drug-treated groups as a function of distance from the nearest neighboring occluded vessel. The data are fitted with a logistic regression with 0.95 confidence intervals. (**i**) Hierarchy of microinfarcts sizes generated by single and multiple vessel occlusions with summary of the pharmacological effect of NMDAR blockers.
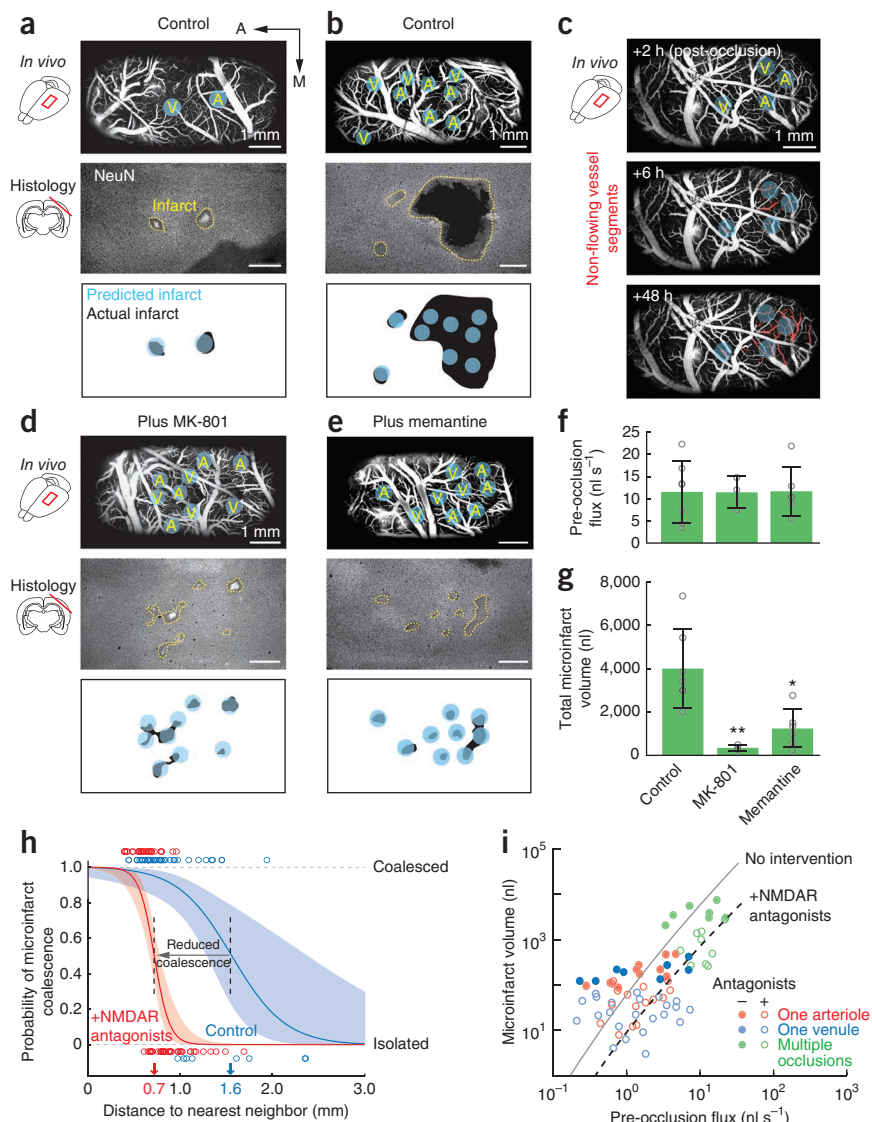
column was suggestive of a mid-point loss of function when only ~0.12 of the column was affected (**Fig. 7e**). This is reminiscent of a 'mass action principle' for sparing of cortical function at the level of a single cortical column, in which the perception of the opposing platform across the gap is a monotonic function of the spared columnar volume[38]. Thus, the extensive reduction in the perceptual deficit by post-occlusion administration of memantine (**Fig. 7f**) was consistent with the concurrent reduction in the size of the microinfarct (**Fig. 5f** and **Supplementary Table 1**).

Coalescence of isolated microinfarcts

Larger infarcts often co-exist with microinfarcts in human *post mortem* brain tissue[4]. Could these have grown from a small set of initially isolated microinfarcts? To test this possibility, we occluded sets of well-separated arterioles and venules to form a multiplicity of microinfarcts in a region of cortex (**Fig. 8**). We observed that the resultant microinfarcts were likely to coalesce when the occlusions were spaced, on average, 1.6 mm or less apart; this corresponds to four to five penetrating vessels in the intervening space between occlusions (**Fig. 8a,b,h**). Furthermore, occlusion of only 5.4 ± 1.1% (mean ± s.d.) of the all of the penetrating vessels in an area of cortex led to complete infarction of the intervening tissue (n = 7; **Fig. 8b**).

The basis of the coalescence of infarcts was revealed through longitudinal imaging studies on animals following occlusion of sets of penetrating vessels. Over a period of 2 d, these clots propagated beyond the initial core of the microinfarct to decrease the perfusion of neighboring penetrating vessels (**Fig. 8c** and **Supplementary Fig. 6**). Coalescence involved severe ischemic damage to the endothelial wall and eventual clot formation in the subsurface microvessels (**Supplementary Fig. 7**). Thus, the cortex appears to be highly susceptible to sparse occlusion of penetrating vessels.

The finding that antagonists of NMDA receptors could decrease the volume of isolated microinfarcts (**Fig. 5**) suggests that the same therapeutic strategy may mitigate the coalescence of microinfarcts. To test this, we formed sets of well-separated single vessel occlusions as described above (**Fig. 8a,b**). MK-801, delivered pre-occlusion, or memantine, delivered post-occlusion, were injected intraperitoneally as described with isolated infarcts. We observed that both antagonists reduced the total volume of infarcted tissue (**Fig. 8d–g**). Coalescence versus isolation of a microinfarct became prevalent when occlusions were placed within 0.7 mm of each other (**Fig. 8d,e,h**), as opposed to the much larger distance of 1.6 mm in the absence of antagonists (**Fig. 8a,b,h**). Thus, the minimum areal density for coalescence was

increased by a factor of five through pharmacological intervention. Longitudinal imaging at the cortical surface of rats treated with MK-801 showed normal flow in surface vessels neighboring targeted vessels (**Supplementary Fig. 8**). Furthermore, a subset of vessels originally occluded by photothrombosis were found to re-cannulate after 1 d, yet this was too late to prevent irreversible damage in the microinfarct core. Taken together, these data indicate that therapeutic administration of NMDAR antagonists has a marked effect on not only the size of isolated microinfarcts, but also on the coalescence of multiple microinfarcts (**Fig. 8i**).

DISCUSSION

The etiology and cognitive consequences of human cortical micro-infarcts are unknown. To gain insight into this issue, we modeled microinfarct pathology (**Fig. 1**) by selective occlusion of individual cortical penetrating arterioles and venules that supply blood to localized regions of tissue in the rat cortex (**Figs. 3** and **4**). We found that microinfarcts were not innocuous, as has been often assumed from their small volume. Instead, the occlusion of only a single penetrating vessel led to cognitive dysfunction in a behavioral task (**Fig. 6**). This implies that every cortical penetrating vessel can be critical for normal cognitive function. Furthermore, we found that an accumulation of multiple microinfarcts led to multiplicative tissue damage (**Fig. 8**), a previously unknown mechanism of cortical injury that may result from small vessel disease. Notably, damage caused by both single and coalesced microinfarctions could be ameliorated with post-occlusion application of memantine, a United States Federal Drug Administration–approved treatment for Alzheimer's disease and vascular dementia[39,40] (**Figs. 5** and **8**). Consistent with the reduction in tissue damage, we observed a large improvement in cognitive function (**Fig. 7**).

The finding that microinfarcts could result from single penetrating venule occlusions was unexpected (**Figs. 3** and **4**) given their nearly three-to-one abundance compared with penetrating arterioles[12]. As with arterioles, there is limited collateral flow between penetrating venules[12], and each venule serves as a sink for the drainage of multiple neighboring penetrating arterioles[41], suggestive of a perfusion domain. In human cortex, that ratio is reversed, with penetrating arterioles outnumbering venules, indicating a larger venular perfusion domain that could be vulnerable to ischemia[42]. In contrast with arterial occlusion, tissue damage caused by venular thrombosis may involve additional mechanisms above ischemia, such as increased intracranial pressure and diapedesis of RBCs[43]. The contribution of venular pathology in dementia is unclear, as markers for vascular identification in *post mortem* neuropathology are not commonly used. Venular collagenosis, which causes narrowing of the lumen, is a presumed source of poor cerebral blood flow in deep white matter, and has been described in vascular dementia[44]. Future efforts to distinguish between arterial and venular pathology in cortex would be valuable, as venular collagenosis can be easily mistaken for more commonly observed hyalinized arterosclerosis[44].

We refined the gap-cross task to involve the use of one macro-vibrissa to sense a target platform (**Fig. 6**) as a means to ascertain the effect of a single microinfarct on cortical function. We found that the occlusion of a single penetrating arteriole was sufficient to disrupt the vibrissa column and abolish the processing of cortical input. This is an important finding, as the behavioral relevance of such small infarcts was previously unknown. This is consistent with the loss of somatosensory maps after small-scale experimental stroke[45]. Indeed, the brain possesses remarkable plasticity and it is likely that, over time, the focal loss of cortical function in this task will be recovered

through remapping of surrounding viable tissue[46,47]. However, an issue of potential clinical importance is whether gradual accumulation of multiple microinfarcts becomes a source of long-term cognitive dysfunction. This possibility is supported by the marked alterations in the flow of neuronal electrical activity between separate cortical areas that occurs subsequent to the occlusion of a single cortical vessel[48].

The lack of flow after occlusion of a penetrating arteriole or venule and the death of nearby tissue (**Fig. 4**) implies that there is poor collateral flow among neighboring penetrating arterioles[11] and penetrating venules[12]. Nonetheless, an unexpected finding was the coalescence of individual microinfarctions into large cysts (**Fig. 8b**). This auto-catalytic-like process can be induced by occlusion of only 5.4% of the total penetrating vessels in a territory, with patent intervening vessels. Blood brain barrier breakdown is unlikely to contribute much to the coalescence effect, as microbleeds[49] and serum extravasation[45] cause little neuronal damage. Rather, delayed thrombosis in the microvasculature may be involved, as recruitment of neighboring penetrating vessels into the ischemic zone occurred approximately 12–24 h after the initial occlusions (**Fig. 8c**). The potential occurrence of microinfarct coalescence in humans as a mechanism of accelerated brain injury remains to be addressed.

We studied microinfarcts in subacute stages where astrogliosis and macrophage infiltration is prominent within the boundaries of the injury and tissue cavitation is incomplete. In later stages, the microinfarct is expected to become a fluid-filled cyst, which eventually collapses to become a linear scar or 'pucker' in chronic stages[3]. Although the optically induced infarcts that we used started on the surface of cortex, microinfarcts that are confined to the bulk of the gray matter occur in humans[2]. Such subsurface microinfarcts could be formed in rodents with the use of amplified, ultrashort laser pulses to block flow in the deep part of a penetrating vessel[50]. High-field magnetic resonance imaging could shed light on the growth of microinfarcts and their correlation with the onset of cognitive decline. Furthermore, different magnetic resonance imaging sequences may be used to estimate the age of microinfarcts on the basis of the sequelae of these changes[2].

The similarity between the vascular architecture and perfusion territory of human penetrating vessels and those of rodents leads to the conjecture that penetrating vessels are the locus of angiopathy leading to microinfarction in humans[9]. This highlights a need for animal models that accurately recapitulate the microvascular dysfunction, tissue pathology and behavioral consequences of vascular dementia. These models will act as test beds for pharmacological interventions, such as prophylactic slow-release anti-excitotoxic strategies, as well as for the development of contrast agents for non-invasive imaging of microinfarcts and longitudinal assessment of new drug treatments based on microinfarct growth. Lastly, it may be appropriate to re-evaluate past neuroprotective therapies for treating ischemic stroke, an abrupt illness, as a means to alleviate dementia, a slowly progressing disease.

METHODS

Methods and any associated references are available in the online version of the paper.

Note: Supplementary information is available in the online version of the paper.

1. Gorelick, P.B. *et al.* Vascular contributions to cognitive impairment and dementia: a statement for healthcare professionals from the American Heart Association/American Stroke Association. *Stroke* **42**, 2672–2713 (2011).
2. Brundel, M., de Bresser, J., van Dillen, J.J., Kappelle, L.J. & Biessels, G.J. Cerebral microinfarcts: a systematic review of neuropathological studies. *J. Cereb. Blood Flow Metab.* **32**, 425–436 (2012).
3. Smith, E.E., Schneider, J.A., Wardlaw, J.M. & Greenberg, S.M. Cerebral microinfarcts: the invisible lesions. *Lancet Neurol.* **11**, 272–282 (2012).
4. Vinters, H.V. *et al.* Neuropathologic substrates of ischemic vascular dementia. *J. Neuropathol. Exp. Neurol.* **59**, 931–945 (2000).
5. Kövari, E. *et al.* Cortical microinfarcts and demyelination affect cognition in cases at high risk for dementia. *Neurology* **68**, 927–931 (2007).
6. Arvanitakis, Z., Leurgans, S.E., Barnes, L.L., Bennett, D.A. & Schneider, J.A. Microinfarct pathology, dementia and cognitive systems. *Stroke* **42**, 722–727 (2011).
7. Jouvent, E. *et al.* Intracortical infarcts in small vessel disease: a combined 7-T postmortem MRI and neuropathological case study in cerebral autosomal-dominant arteriopathy with subcortical infarcts and leukoencephalopthy. *Stroke* **42**, 27–30 (2011).
8. Blinder, P., Shih, A.Y., Rafie, C.A. & Kleinfeld, D. Topological basis for the robust distribution of blood to rodent neocortex. *Proc. Natl. Acad. Sci. USA* **107**, 12670–12675 (2010).
9. Lauwers, F., Cassot, F., Lauwers-Cances, V., Puwanarajah, P. & Duvernoy, H. Morphometry of the human cerebral cortex microcirculation: general characteristics and space-related profiles. *Neuroimage* **39**, 936–948 (2008).
10. Bär, T. The vascular system of the cerebral cortex. *Adv. Anat. Embryol. Cell Biol.* **59**, 1–62 (1980).
11. Nishimura, N., Schaffer, C.B., Friedman, B., Lyden, P.D. & Kleinfeld, D. Penetrating arterioles are a bottleneck in the perfusion of neocortex. *Proc. Natl. Acad. Sci. USA* **104**, 365–370 (2007).
12. Nguyen, J., Nishimura, N., Fetcho, R.N., Iadecola, C. & Schaffer, C.B. Occlusion of cortical ascending venules causes blood flow decreases, reversals in flow direction, and vessel dilation in upstream capillaries. *J. Cereb. Blood Flow Metab.* **31**, 2243–2254 (2011).
13. Drew, P.J. *et al.* Chronic optical access through a polished and reinforced thinned skull. *Nat. Methods* **7**, 981–984 (2010).
14. Sofroniew, M.V. & Vinters, H.V. Astrocytes: biology and pathology. *Acta Neuropathol.* **119**, 7–35 (2010).
15. Tsai, P.S. *et al.* Correlations of neuronal and microvascular densities in murine cortex revealed by direct counting and colocalization of cell nuclei and microvessels. *J. Neurosci.* **29**, 14553–14570 (2009).
16. Weber, B., Keller, A.L., Reichold, J. & Logothetis, N.K. The microvascular system of the striate and extrastriate visual cortex of the macaque. *Cereb. Cortex* **18**, 2318–2330 (2008).
17. Svoboda, K., Denk, W., Kleinfeld, D. & Tank, D.W. *In vivo* dendritic calcium dynamics in neocortical pyramidal neurons. *Nature* **385**, 161–165 (1997).
18. Kleinfeld, D., Mitra, P.P., Helmchen, F. & Denk, W. Fluctuations and stimulus-induced changes in blood flow observed in individual capillaries in layers 2 through 4 of rat neocortex. *Proc. Natl. Acad. Sci. USA* **95**, 15741–15746 (1998).
19. Shih, A.Y. *et al.* Active dilation of penetrating arterioles restores red blood cell flux to penumbral neocortex after focal stroke. *J. Cereb. Blood Flow Metab.* **29**, 738–751 (2009).
20. Shih, A.Y. *et al.* Two-photon microscopy as a tool to study blood flow and neurovascular coupling in the rodent brain. *J. Cereb. Blood Flow Metab.* **32**, 1277–1309 (2012).
21. Schaffer, C.B. *et al.* Two-photon imaging of cortical surface microvessels reveals a robust redistribution in blood flow after vascular occlusion. *PLoS Biol.* **4**, e22 (2006).
22. Nishimura, N. *et al.* Targeted insult to individual subsurface cortical blood vessels using ultrashort laser pulses: three models of stroke. *Nat. Methods* **3**, 99–108 (2006).
23. Stosiek, C., Garaschuk, O., Holthoff, K. & Konnerth, A. *In vivo* two-photon calcium imaging of neuronal networks. *Proc. Natl. Acad. Sci. USA* **100**, 7319–7324 (2003).
24. Chen, B. *et al.* Severe blood brain barrier disruption and surrounding tissue injury. *Stroke* **40**, 666–674 (2009).
25. Calabrese, V., Mancuso, C., Calvani, M., Rizzarelli, E. & Butterfield, D.A. Nitric oxide in the central nervous system: neuroprotection versus neurotoxicity. *Nat. Rev. Neurosci.* **8**, 766–775 (2007).
26. Friedman, B. *et al.* Acute vascular disruption and Aquaporin 4 loss after stroke. *Stroke* **40**, 2182–2190 (2009).
27. Unal Cevik, I. & Dalkara, T. Intravenously administered propidium iodide labels necrotic cells in the intact mouse brain after injury. *Cell Death Differ.* **10**, 928–929 (2003).
28. Soontornniyomkij, V. *et al.* Cerebral microinfarcts associated with severe cerebral beta-amyloid angiopathy. *Brain Pathol.* **20**, 459–467 (2010).
29. Siesjö, B.K. & Bengtsson, F. Calcium fluxes, calcium antagonists and calcium-related pathology in brain ischemia, hypoglycemia, and spreading depression: a unifying hypothesis. *J. Cereb. Blood Flow Metab.* **9**, 127–140 (1989).
30. Murphy, T.H., Li, P., Betts, K. & Liu, R. Two-photon imaging of stroke onset *in vivo* reveals that NMDA receptor–independent ischemic depolarization is the major cause of rapid reversible damage to dendrites and spines. *J. Neurosci.* **28**, 1756–1772 (2008).
31. Orgogozo, J.M., Rigaud, A.S., Stoffler, A., Mobius, H.J. & Forette, F. Efficacy and safety of Memantine in patients with mild to moderate vascular dementia. *Stroke* **33**, 1834–1839 (2002).
32. Olivares, D. *et al.* N-Methyl D-Aspartate (NMDA) receptor antagonists and memantine treatment for Alzheimer's disease, vascular dementia and Parkinson's disease. *Curr. Alzheimer Res.* **9**, 746–758 (2012).
33. Woolsey, T.A. & Van Der Loos, H. The structural organization of layer IV in the somatosensory region (SI) of mouse cerebral cortex. *Brain Res.* **17**, 205–242 (1970).
34. Kleinfeld, D. & Deschênes, M. Neuronal basis for object location in the vibrissa scanning sensorimotor system. *Neuron* **72**, 455–468 (2011).
35. Hutson, K.A. & Masterton, R.B. The sensory contribution of a single vibrissa's cortical barrel. *J. Neurophysiol.* **56**, 1196–1223 (1986).
36. Masino, S.A., Kwon, M.C., Dory, Y. & Frostig., R.D. Characterization of functional organization within rat barrel cortex using intrinsic signal optical imaging through a thinned skull. *Proc. Natl. Acad. Sci. USA* **90**, 9998–10002 (1993).
37. Armstrong-James, M., Fox, K. & Das-Gupta, A. Flow of excitability within barrel cortex on striking a single vibrissa. *J. Neurophysiol.* **68**, 1345–1358 (1992).
38. Lashley, K.S. Mass action in cerebral function. *Science* **73**, 245–254 (1931).
39. Reisberg, B. *et al.* Memantine in moderate-to-severe Alzheimer's disease. *N. Engl. J. Med.* **348**, 1333–1341 (2003).
40. Wilcock, G.K. Memantine for the treatment of dementia. *Lancet Neurol.* **2**, 503–505 (2003).
41. Woolsey, T.A. *et al.* Neuronal units linked to microvascular modules in cerebral cortex: response elements for imaging the brain. *Cereb. Cortex* **6**, 647–660 (1996).
42. Cassot, F. *et al.* Branching patterns for arterioles and venules of the human cerebral cortex. *Brain Res.* **1313**, 62–78 (2010).
43. Villringer, A., Mehraein, S. & Einhäupl, K.M. Pathophysiological aspects of cerebral sinus venous thrombosis (SVT). *J. Neuroradiol.* **21**, 72–80 (1994).
44. Brown, W.R. & Thore, C.R. Cerebral microvascular pathology in aging and neurodegeneration. *Neuropathol. Appl. Neurobiol.* **37**, 56–74 (2011).
45. Zhang, S. & Murphy, T.H. Imaging the impact of cortical microcirculation on synaptic structure and sensory-evoked hemodynamic responses *in vivo*. *PLoS Biol.* **5**, e119 (2007).
46. Troncoso, E. *et al.* Recovery of evoked potentials, metabolic activity and behavior in a mouse model of somatosensory cortex lesion: role of the neural cell adhesion molecule (NCAM). *Cereb. Cortex* **14**, 332–341 (2004).
47. Carmichael, S.T. Plasticity of cortical projections after stroke. *Neuroscientist* **9**, 64–75 (2003).
48. Mohajerani, M.H., Aminoltejari, K. & Murphy, T.H. Targeted mini-strokes produce changes in interhemispheric sensory signal processing that are indicative of disinhibition within minutes. *Proc. Natl. Acad. Sci. USA* **108**, E183–E191 (2011).
49. Rosidi, N.L. *et al.* Cortical microhemorrhages cause local inflammation but do not trigger widespread dendrite degeneration. *PLoS ONE* **6**, e26612 (2011).
50. Nishimura, N., Rosidi, N.L., Iadecola, C. & Schaffer, C.B. Limitations of collateral flow after occlusion of a single cortical penetrating arteriole. *J. Cereb. Blood Flow Metab.* **30**, 1914–1927 (2010).

ONLINE METHODS

Animal preparation. We used 220 male rats (Charles River), ranging in mass from 250–400 g and maintained in standard cages on a natural light-dark cycle. We used 80 Sprague Dawley rats for in physiological and anatomical measurements and 140 Long Evans rats for behavioral experiments, of which 20 of the 140 completed training to yield useful data. The care and experimental manipulation of our rats was approved by the Institutional Animal Care and Use Committee at the University of California at San Diego.

All reagents were acquired from Sigma unless otherwise noted. Surgeries were performed under isoflurane (Baxter Healthcare) anesthesia, 4% mean alveolar concentration (MAC) in 30% oxygen and 70% nitrous oxide for induction and 1–2% MAC for maintenance. Body temperature was maintained at 37 °C with a feedback-regulated heat pad (50-7053-F, Harvard). Heart rate and blood oxygen saturation were continuously monitored using a pulse oximeter (8,600 V, Nonin). Intraperitoneal injections of 5% glucose (wt/vol) in 1 ml saline were given every 2 h for rehydration. Buprenorphine (0.02 mg per kg of body weight) was administered intraperitoneally for post-operative analgesia.

For acute studies (**Figs. 2b** and **3a–e,i**), the femoral artery was cannulated for continuous measurement of blood pressure (BP1, World Precision Instruments) and withdrawal of blood for blood gas analysis (RapidLab 248, Bayer), and the femoral vein was similarly cannulated for delivery of reagents, such as fluorescein-dextran, Rose Bengal and anesthetic. Prior to imaging, isoflurane was discontinued and anesthesia was transitioned to α-chloralose with an intravenous bolus injection of 50 mg per kg in saline, and then maintained with a steady flow of 40 mg per kg per h with a syringe pump. For survival studies (**Figs. 1b**, **3f–h**, **4**, **5** and **8**), rats were maintained only on isoflurane for the duration of the surgery and imaging. In these cases, the femoral artery and vein were cannulated more distally to minimize disruption of blood flow in the leg. Given that femoral artery catheters could affect locomotion, that rats used in behavioral experiments (**Figs. 6** and **7**) were catheterized only in the distal femoral vein for delivery of reagents.

Dura-removed cranial windows were generated over the somatosensory cortex, as described previously[20]. Cranial windows were centered on ±3 mm mediolateral and –0.5 mm anteroposterior for imaging of the hindlimb/forelimb sensory cortex, and +5.5 mm mediolateral and –3 mm anteroposterior for vS1.

Drug preparation and administration. The NMDAR antagonists MK-801 (Tocris) and Memantine (Tocris) were dissolved in sterile phosphate-buffered saline (PBS) and stored at 20 °C. MK-801 at a concentration of 1 mg per kg was administered 30 min before the initiation of vessel occlusion, and memantine at a concentration of 20 mg per kg was administered 30 min after initiation of occlusion. Both drugs were administered intraperitoneally as a single bolus. After drug administration, the rats were placed in a cage warmed to 32 °C for 4 h to avoid possible hypothermia. Drug administration did not significantly alter the measured physiological variables (**Supplementary Table 2**).

Somatosensory cortex mapping. The sensory cortex was mapped by intrinsic optical imaging of blood de-oxygenation[51]. After craniotomy and durectomy, the exposed cortex was temporarily covered with agarose and a coverslip[20]. For identification of limb representations, the limb was electrically stimulated with a 0.5–1 mA, 10-ms pulse width, 3-Hz, 3-s train of pulses. For identification of vS1 cortical columns, single vibrissae were mechanically stimulated with a piezoelectric actuator under light isoflurane anesthesia[36]. Images of a 3- × 3-mm area were acquired with a macroscope[52] fitted with a 12-bit CMOS camera (no. 1M60, Dalsa); the data were binned into 256 × 256 pixel frames at 2 frames per s for analysis. An initial image of the cortical surface vasculature made use of illumination by 475-nm center wavelength light-emitting diodes (LEDs), which formed a reference to relate functional changes to specific locations in the window. Functional images were then obtained by illuminating the cortical surface with 630-nm center wavelength LEDs.

***In vivo* two-photon microscopy.** Measurements of vascular structure, blood flow and intracellular [Ca2+] transients made use of a custom-designed two-photon laser-scanning microscope[53] with arbitrary scan patterns[54,55] that further supported additional beams for linear[21] and nonlinear[22] thrombosis of single small vessels by focused lasers[56]. Control of scanning and data acquisition was achieved through the MPScope 2.0 software system[57]. The blood serum was labeled by

intravenous injection of 0.3 ml of 2 MDa fluorescein-dextran (FD2000S, Sigma) prepared at a concentration of 5% (wt/vol) in saline. Procedures for blood flow measurement and analysis have been described previously[20].

Calcium imaging. The membrane-permeant [Ca2+] indicator OGB1-AM (Invitrogen) was bolus-loaded into cortex as described previously[23]. Astrocytes were selectively labeled with sulforhodamine 101 (SR101)[58]. A 0.8-NA, 40× water-dipping objective was used for imaging. The excitation wavelength was 800 nm, and the collection band of OGB1 fluorescence was 350–570 nm and that of SR101 was 570–680 nm. Images were 400 × 256 pixels in size, and a time series consisted of 300 frames collected at 10 Hz. A single 0.5–1-mA, 10-ms pulse was applied to the hindlimb or forelimb to induce neuronal firing at frame 100 in each series. Data sets were collected once before occlusion and at various times post-occlusion. Each data set consisted of five different depths ranging from 200–400 μm below the surface (50-μm intervals), with five series collected at each depth. Mean arterial blood pressure, blood gases and blood pH were maintained at normal physiological levels throughout the Ca2+ imaging and acute blood flow experiments.

Targeted occlusion of individual vessels. Penetrating vessels were occluded on the cortical surface by focal activation of the circulating photosensitizer, Rose Bengal, with a green laser (Crystalaser)[21]. Deep microvessels were occluded using an amplified 800-nm pulsed laser (Libra, Coherent)[22]. Technical and experimental details for both occlusion techniques have been described previously[56].

Immunohistology. Rats were perfusion fixed with 4% paraformaldehyde (wt/vol). Brains were post-fixed overnight at 4 °C followed by equilibration with 30% sucrose (wt/vol). For most cases, the entire ipsilateral cortex was removed and sandwiched between two glass slides separated by a distance of 2.5 mm before post-fixation. Brain sections, 50 μm thick, were then cut tangential to the cortical surface with a sliding microtome. Primary antibodies (**Supplementary Table 3**) were diluted in buffer that consisted of 10% goat serum (vol/vol, Vector Labs), 2% Triton X-100 (vol/vol) and 0.2% sodium azide (wt/vol). Free-floating sections were then incubated overnight under slow rotation at 20 °C in an antibody solution, washed in 50 ml of PBS for 30 min on an orbital shaker, incubated with secondary antibody (**Supplementary Table 3**) for 2 h, washed again, mounted and dried on slides overnight. All slides were then sealed with Fluoromount-G (Southern Biotechnology Associates) and a No. 1 glass coverslip (Corning).

For pimonidazole hydrochloride (Hypoxyprobe) immunostaining of hypoxic tissue[19], pimonidazole was injected through the femoral artery catheter 1 h before perfusion fixation at a concentration of 60 mg per kg in a volume of 100 μl saline. For labeling of necrotic tissue, propidium iodide was injected intraperitoneally 2 h before perfusion fixation, at a concentration of 1 mg per kg in a volume of 1 ml saline[27].

Macrovibrissa-dependent behavioral testing. The gap-cross apparatus consisted of two polyvinyl chloride platforms, shaped as isosceles trapezoids 20 cm wide in back, 10 cm wide in front, and 25 cm long, that faced each other on their short sides and were raised 50 cm above a table. The three non-opposing sides were enclosed with clear plastic and covered with a plastic roof to prevent the rats from exploring the other edges of the platform. Small wells were drilled into the far end of either platform and served as reward ports. Flow to each well was controlled by a solenoid that released 120 μl of water sweetened with 0.02% saccharin (wt/vol) per spritz from a pressurized water bottle. Stepping motor controllers (no. UCC3055, Norberg) were installed at the base of each platform to allow the gap distance to be changed mechanically.

Rat centroid tracking. The platforms were located 30 cm in front of a flat black screen and illuminated by diffuse reflected light from two LEDs (M850 nm, ThorLabs). An infrared-sensitive CCD camera (no. C3077-79, Hamamatsu) with a side view of the platform collected data at 60 frames per s. As the rat crossed back and forth between platforms for water rewards, its position was evaluated by computing the centroid of the image intensity. A crossing event was registered when the rat centroid crossed the gap and moved 2.5 cm beyond the edge of the target platform. The platform that the rat had crossed from was then repositioned to define a new gap distance; platforms were never repositioned

while the rats were on them. Occasionally, the rat would return back to the initial platform before the stages had fully repositioned. These crossings were flagged and omitted during post-processing. All computation and control made use of MATLAB-based programs that processed the camera output, controlled the platform motors, and triggered the solenoids[59].

Macrovibrissa tracking. The macrovibrissae were imaged from overhead as the animals perched across the gap to palpate the target platform. We used a high-speed camera (Basler A602f) fitted with an $f = 50$-mm lens (Olympus f/1.2 Auto-S) located 80 cm above the platform. The camera was fixed to a separate stepping motor that was synchronized to move with the edge of the right platform. Frames were acquired 250 times per s. Two additional LEDs (M850 nm, ThorLabs) provided diffuse illumination of the gap region from below. The LEDs illuminated the flat-white interior of a 15-cm diameter by 10-cm-long cylindrical tube with an aperture placed below the edge of the right platform.

Training procedure. Rats were deprived of water 24 h before their first run. As a first step, they were trained to run between the platforms in dim visible light with a bridge to fill the gap. Each successful cross triggered the solenoid on the target platform to release a water reward. Rats that crossed 50 times or more their first day on the apparatus were kept as candidates for further training, and the remainder were culled.

The successful animals were then trained to run between platforms separated by a small gap of 3–6 cm. Once they were comfortable crossing, the computer control was set to increase the gap width by an interval of 0.1 cm after every successful cross. Once they reached a gap they could not cross within a period of 120 s, the space would be reduced by several centimeters and the process would repeat. Using this 'staircase' method, the rats were trained to cross gaps of increasing size.

Once the rats were proficient at the staircase method, they were run in the same task under infrared light, which was invisible to the rats. Initially, they were found to cross a gap only if the other platform was reachable with a front paw. With time, they gained the confidence to cross larger distances by stretching their upper torsos over the gap to touch the target platform with the snout. Finally, they learned to use their macrovibrissae to feel the edge of the target platform when it was past their snout, typically at a gap distance of 14 to 18 cm, which depended on the size of the rat. Training included randomly placed blank trials[35], where the gap distance was increased to a value larger than the rat could probe with its macrovibrissa. If the rat tried to jump the gap during such trials, it fell to a cushion on the table. This adverse experience assured that it would not jump without actively probing for the target platform in future trials. Falling during a blank trial was a necessary event for all trained rats, as it reinforced the need to palpate before crossing. Approximately 30% of the initial rats achieved this level of training.

Reducing the number of macrovibrissae to one. We found that rats trimmed to only a single macrovibrissa before the initial training failed to learn to use the macrovibrissa for the task. Thus, we allowed rats to learn the task with a full set of macrovibrissae, which were then sequentially trimmed. The first trim removed all macrovibrissae ipsilateral to the eventual microinfarct, the second trim removed the macrovibrissae in rows A and E on the contralateral side, the third trim removed the macrovibrissae in rows B and D, and the fourth trim removed all remaining macrovibrissae except C1 and C2. For the final trim, we used the high-speed macrovibrissa tracking data to determine which of the last two the rat was more reliant on for gap crossing and trimmed the other. After each trim, the rat was run until its performance recovered to values achieved before trimming; this typically required an additional 1–3 d of training. Approximately 15% of the initial rats achieved this level of training.

Psychometric testing program. After training, the rats were tested on the gap-crossing task using a probabilistic assessment of their abilities. Control software randomly selected one of five preset gap widths for each trial, which assured that the rat could not predict the next gap width. The highest width was set to one that the rat was not able to cross with its macrovibrissae because it was 1 cm out of reach, and the other four were successively 1 cm lower. The optimal range of gap distances for each rat was found empirically. Each run consisted of 80–120 trials, challenging the rat at least 15 times per gap distance. The number of successful

crosses per gap distance returned a probability of crossing for each width (**Fig. 6f**). The deficit caused by a manipulation was calculated as the difference between curves at the 0.5-chance of crossing.

Pre-occlusion baseline. Three to four runs were used to establish a pre-occlusion baseline.

Post-occlusion data collection. Rats were given water *ad libitum* the night before surgery for vessel occlusion and for 1 d following surgery. Starting 2 d after the formation of an occlusion (**Supplementary Fig. 5**), the rat were run for an additional four to seven sessions to develop a post-occlusion baseline.

Macrovibrissa trim control. Once a stable post-occlusion baseline was established, the single remaining macrovibrissa was trimmed to its base. The rats were then run to establish a macrovibrissa-free baseline that served as a control.

All rats maintained ~90% of their original body weight over the duration of the study. They were run once every day, and were only given water from the apparatus.

Statistics. For the composite data shown in **Figures 3c–e, 6g,k** and **7d**, we used a repeated-measures ANOVA and a Tukey *post hoc* analysis. For the composite data shown in **Figures 5d,e, 7f** and **8f,g**, we used the Kruskal Wallis test and a Dunn's *post hoc* analysis.

Infarct volume. To quantify microinfarct volumes, we used α-NeuN–stained tissue sections. Serial images of the microinfarct were collected at high-resolution with a stereoscope (MVX10, Olympus). The microinfarct boundary was delineated as the border between normal tissue exhibiting dense neuronal nuclei and infarcted regions devoid of nuclei (**Supplementary Fig. 4a,b**). Nonspecific NeuN immunostaining in the microinfarct core, likely resulting from undigested tissue matter, was easily distinguished from neuronal nuclei based on morphology. The area of tissue damage was measured in adjacent tissue sections and the total infarct volume, V_t, was calculated by $V_t = (A_1 + A_2 + . + A_n)h$, where A_n was the area of damage in the nth slice, and h was the distance between adjacent sections. With extremely small lesions caused by deep microvessel thrombosis, the damage was often limited to only a single slice (**Fig. 4e** and **Supplementary Fig. 1e,f**). In these cases, the volume of propidium iodide–positive tissue was measured with a confocal microscope using a 1-μm step size (Olympus FV1000).

The volume of a vS1 cortical column was estimated as the area of the column at the level of layer 4, based on VGLUT2 immunostaining (**Figs. 6e,i** and **7b** and **Supplementary Fig. 5h**), times the thickness of cortex at that level of bregma, 2.2 mm[60]. The area of the column was measured separately for each rat. For rats with the column completely infarcted, the area was estimated by averaging the area of two to three neighboring columns that remained intact. Fractional damage (**Fig. 7e**) was computed by dividing the volume of infarcted tissue in the column by the total volume of the column. A mask of the column, derived at layer 4, was applied to all sections to delineate the column boundary through the depth of cortex. Deep penetrating vessels, identified as holes in a tangential slice, were used as fiducial markers for alignment of serial sections.

Calcium imaging analysis. Calcium indicator fluorescence from cell somata was extracted from planar image stacks using a supervised machine learning algorithm[54]. We excluded from analyses cells that were positively stained for SR101 in a second imaging channel and fluorescein-dextran–containing vessel segments. The [Ca2+] transients from individual neurons, indicative of action potential firing, exhibited an effectively instantaneous increase followed by an exponential decay over a 1–2-s period (**Fig. 3b**). We identified the onset of the transient by matched filtering with an idealized exponential decay, $e^{-(t-t_n)/\tau}\theta(t - t_n)$, where $\theta(t)$ is the Heaviside function, t_n is the putative event time and $\tau = 300$ ms. To be scored as a significant increase in [Ca2+] over baseline signal, the correlation between the data and the filter was required to be at least 2σ above zero, with σ defined across a population of 1,000 trace segments randomly collected from non-stimulation periods in the same data sets.

51. Frostig, R.D., Lieke, E.E., Ts'o, D.Y. & Grinvald, A. Cortical functional architecture and local coupling between neuronal activity and the microcirculation revealed by *in vivo* high-resolution optical imaging of intrinsic signals. *Proc. Natl. Acad. Sci. USA* **87**, 6082–6086 (1990).

52. Kleinfeld, D. & Delaney, K.R. Distributed representation of vibrissa movement in the upper layers of somatosensory cortex revealed with voltage sensitive dyes. *J. Comp. Neurol.* **375**, 89–108 (1996).

53. Tsai, P.S. & Kleinfeld, D. *In vivo* two-photon laser scanning microscopy with concurrent plasma-mediated ablation: principles and hardware realization. in *Methods for In Vivo Optical Imaging* 2nd edn. (ed. Frostig, R.D.) 59–115 (CRC Press, 2009).

54. Valmianski, I. *et al.* Automatic identification of fluorescently labeled brain cells for rapid functional imaging. *J. Neurophysiol.* **104**, 1803–1811 (2010).

55. Driscoll, J.D., Shih, A.Y., Drew, P.J., Cauwenberghs, G. & Kleinfeld, D. Two-photon imaging of blood flow in cortex. in *Imaging in Neuroscience: A Laboratory Manual* (eds. Helmchen, F., Konnerth, A. & Yuste, R.) 927–938 (Cold Spring Harbor Laboratory Press, New York, 2011).

56. Shih, A.Y. *et al.* Optically induced occlusion of single blood vessels in neocortex. in *Imaging in Neuroscience: A Laboratory Manual* (eds. Helmchen, F., Konnerth, A. & Yuste, R.) 939–948 (Cold Spring Harbor Laboratory Press, New York, 2011).

57. Nguyen, Q.-T., Dolnick, E.M., Driscoll, J. & Kleinfeld, D. MPScope 2.0: A computer system for two-photon laser scanning microscopy with concurrent plasma-mediated ablation and electrophysiology. in *Methods for In Vivo Optical Imaging* 2nd edn. (ed. Frostig, R.D.) 117–142 (CRC Press, 2009).

58. Nimmerjahn, A., Kirchhoff, F., Kerr, J.N. & Helmchen, F. Sulforhodamine 101 as a specific marker of astroglia in the neocortex *in vivo*. *Nat. Methods* **1**, 31–37 (2004).

59. Mehta, S.B., Whitmer, D., Figueroa, R., Williams, B.A. & Kleinfeld, D. Active spatial perception in the vibrissa scanning sensorimotor system. *PLoS Biol.* **5**, 309–322 (2007).

60. Paxinos, G. & Watson, C. *The Rat Brain in Stereotaxic Coordinates* (Academic Press, San Diego, 1986).